

**Strong exciton-polariton correlations shape the many-body
polariton dynamics in two-dimensional metal halide
semiconductor microcavities: Competitive pathways for polariton
condensation**

Victoria Quirós-Cordero,^{1,*} Esteban Rojas-Gatjens,^{2,3,*} Martín Gómez-Dominguez,¹
Hao Li,^{4,5} Carlo A. R. Perini,¹ Natalie Stingelin,^{1,6} Eric R. Bittner,⁴
Juan-Pablo Correa-Baena,¹ Ajay Ram Srimath Kandada,^{7,†} and Carlos Silva-Acuña^{1,2,3,5,‡}

¹*School of Materials Science and Engineering, Georgia Institute of Technology,
771 Ferst Dr NW, Atlanta, GA 30332, United States*

²*School of Chemistry and Biochemistry, Georgia Institute of Technology,
901 Atlantic Drive, Atlanta, GA 30332, United States*

³*School of Physics, Georgia Institute of Technology,
837 State St NW, Atlanta, GA 30332, United States*

⁴*Department of Physics, University of Houston,
Houston, Texas 77204, United States*

⁵*Institut Courtois & Département de physique,
Université de Montréal, 1375 Avenue Thérèse-Lavoie-Roux,
Montréal H2V 0B3, Québec, Canada*

⁶*School of Chemical and Biochemical Engineering,
Georgia Institute of Technology, 311 Ferst Dr, Atlanta, GA 30332, United States*

⁷*Department of Physics & Center for Functional Materials,
Wake Forest University, Winston-Salem,
North Carolina 27109, United States*

(Dated: April 24, 2024)

Abstract

Polariton condensation relies on the massive occupation of the lowest-energy polariton state beyond a required critical density. The mechanisms driving both the occupation and depopulation of the lowest-energy polariton state all rely on multi-particle scattering, and its dynamics determine the extent to which condensates can form spontaneously. To pinpoint many-body processes hindering polariton condensation in two-dimensional metal-halide semiconductors, we examine the exciton-polariton dynamics in a Fabry-Pérot microcavity over timescales involving the dynamics of multi-particle polariton ($\ll 1$ ps) and exciton scattering processes ($\gg 1$ ps). We find evidence of enhanced nonlinear exciton-exciton scattering in the microcavity compared to that in the semiconductor, and that the exciton reservoir mediates polariton scattering. We posit that the complex scattering landscape between the exciton reservoir and polaritons limits the formation of polariton condensates in two-dimensional metal-halide semiconductors, and we discuss the generality of our conclusions for materials systems in which the lattice mediates strong multi-particle correlations.

* V.Q.C. and E.R.G. are first co-authors

† srimatar@wfu.edu

‡ carlos.silva@umontreal.ca

Exciton-polaritons are hybrid light-matter quasiparticles present in systems with non-dissipative, coherent energy exchange — i.e., strong light-matter coupling — between excitons in a semiconductor and a confined electromagnetic field. Due to their nonlinear optical response [1, 2] and their capacity to spontaneously form quantum phases with macroscopic coherence, known as polariton condensates [3–5], these quasiparticles are at the forefront for the realization of low-threshold lasers [6, 7] and light-emitters [8, 9], optical circuitry and logic gates [10, 11], as well as quantum information technologies [12].

Upon nonresonant excitation, strong coupling between N excitons and an optical-mode radiation leads to polariton states and a residual excitonic background, known as the *exciton reservoir* (Fig. 1). The reservoir has been mostly regarded as an intermediate pathway to populate polaritons via incoherent processes like radiative pumping [13–15] or the emission of a phonon or vibron [16–18]. Radiative pumping has been reported as the main mechanism for polariton population organic [13] and in two-dimensional metal-halide microcavities [14, 15]. Nevertheless, recent work suggests that the exciton reservoir might play a more active role; for instance, Payta *et al.* [19] proposed that the delocalization of the reservoir influences the propagation dynamics of exciton-polaritons in organic microcavities.

The ensemble of uncorrelated polaritons, populated through the exciton reservoir, must massively feed the lowest-energy $\vec{k}_{\parallel} = \vec{0}$ state and achieve a critical population density, at which the wavefunction of polaritons overlaps to form a condensate. For the latter, one needs: (i) efficient population of the polariton $\vec{k}_{\parallel} = \vec{0}$ state, (ii) amplification of this population rate (i.e., bosonic enhancement), and (iii) for the relaxation towards the lower polariton $\vec{k}_{\parallel} = \vec{0}$ state to be more efficient than depopulation mechanisms, which include the emission rate of the condensate, thermal depletion, and quantum depletion [20, 21]. The latter competition also plays a key role in the lifetime of polariton condensates.

In our previous work, we characterized multi-exciton correlations in two-dimensional metal-halide semiconductors, which manifest as excitation-induced dephasing and biexciton signatures in the nonlinear coherent optical response [22–25]. Here, we characterize the nonlinear many-body interactions within a $(\text{PEA})_2\text{PbI}_4$ (PEA: phenylethylammonium) Fabry-Pérot microcavity exhibiting multiple (upper, middle, and lower) polariton states due to various excitonic species of the semiconductor [26–28] coupling with the microcavity optical mode. We probe many-body interactions at the timescale of both the exciton and polariton lifetimes. The nonlinear photoluminescence evidences an increased exciton-exciton anni-

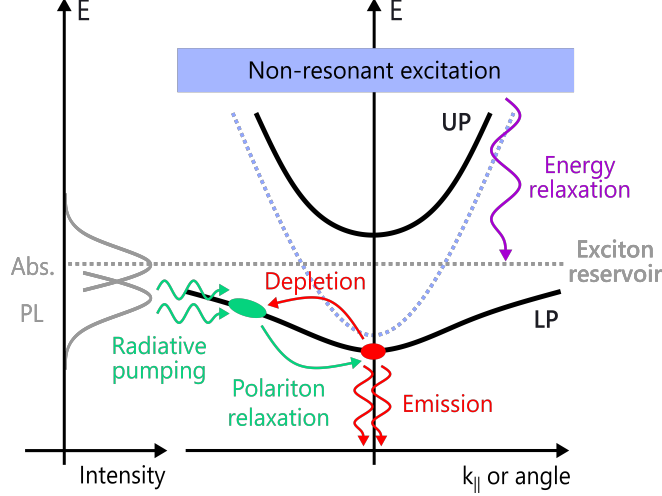


FIG. 1. Competing mechanisms to populate the lower polariton $\vec{k}_{\parallel} = \vec{0}$ state, under a non-resonant excitation, in two-dimensional metal-halide semiconductors.

hilation in the exciton reservoir. Additionally, via two-dimensional coherent spectroscopy, we observe both an ultrafast population transfer from the exciton reservoir and the middle polariton to the lower polariton state and a depletion of the lower polariton from $\vec{k}_{\parallel} = 0$ to higher energy, larger in-plane momentum states over a ~ 100 fs timescales. Finally, we identify the exciton reservoir as a scattering bath for the lower polaritons through two quantum coherent spectroscopy. These results reveal strong correlations between the exciton reservoir and exciton-polaritons in two-dimensional metal halides, which dictate the population, depletion, and scattering of polaritons in both femtosecond and picosecond timescales.

I. RESULTS

A. Exciton-polaritons in $(\text{PEA})_2\text{PbI}_4$

A schematic of the microcavity studied in this work and the structure of $(\text{PEA})_2\text{PbI}_4$ are included in Fig. 2(a). The energy dispersion of the microcavity shows four bands with reflectance local minima corresponding to an upper, two middle, and a lower polariton branch (dark blue features in the right panel of Fig. 2(b)). The multiple polariton states arise from the coupling of the microcavity optical mode ($E_{\text{Opt.}}$) with the various excitonic features of $(\text{PEA})_2\text{PbI}_4$ [26–28]. The low-temperature absorption spectrum of the bare semiconductor (top black solid line in the left panel of Fig. 2(b)) evidences three excitonic features labeled

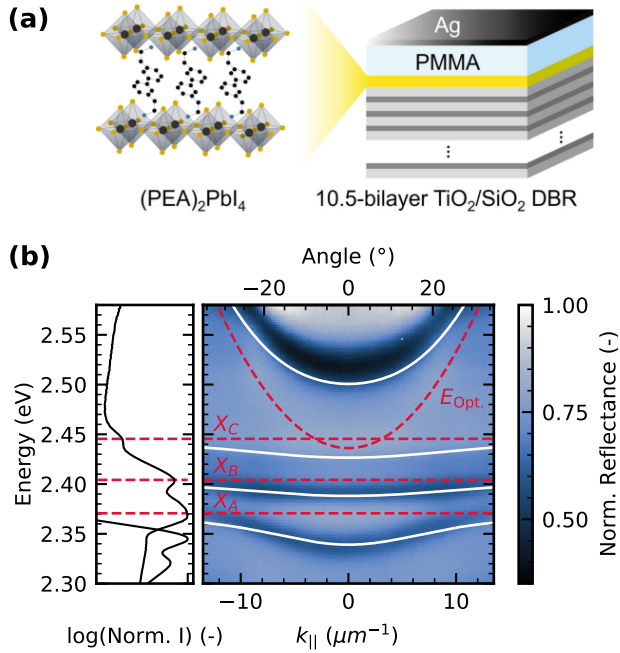


FIG. 2. Two-dimensional lead-iodide Fabry-Pérot microcavity. (a) The microcavity comprises a bottom 520 nm quarter-wave distributed Bragg reflector (made of 10.5 bilayers of $\text{TiO}_2/\text{SiO}_2$ represented in dark and light gray, respectively), a 60 nm $(\text{PEA})_2\text{PbI}_4$ film, a 125 nm poly(methyl methacrylate) spacer layer, and a 40 nm Ag film serving as a semitransparent top mirror. (b) The energy dispersion relation measured at 5 K with Fourier microscopy (right panel) shows an upper, two middle, and a lower polariton branch, distinct from the microcavity mode E_{Opt} . and the excitons X_A , X_B , and X_C . The polariton branches observed agree with the eigenstates of the Hamiltonian described in equations (1) and (2) (solid white lines). The left panel includes the absorption (top) and photoluminescence (bottom) spectra of a 60 nm $(\text{PEA})_2\text{PbI}_4$ film in a logarithmic scale showing the three excitonic features.

X_A , X_B , and X_C . In our previous work, we interpreted the spectral structure as a family of exciton-polarons with distinct exciton-phonon coupling, although we note other researchers interpret it as a vibronic progression [26–28]. The energy dispersion of the microcavity agrees with the eigenstates of a Hamiltonian (white solid lines in Fig. 2.(b)) which includes the three excitons coupling independently to a unique optical mode, detailed in equations (1) and (2).

$$H(\vec{k}_{\parallel}) = \hbar\omega_A b_A^\dagger b_A + \hbar\omega_B b_B^\dagger b_B + \hbar\omega_C b_C^\dagger b_C + \hbar\omega_P(\vec{k}_{\parallel}) a_P^\dagger a_P + V_{\text{coup}}. \quad (1)$$

$$V_{\text{Coup.}} = g_A(a_P^\dagger b_A + a_P b_A^\dagger) + g_B(a_P^\dagger b_B + a_P b_B^\dagger) + g_C(a_P^\dagger b_C + a_P b_C^\dagger) \quad (2)$$

Here, $\hbar\omega_i$ corresponds to the energy of the excitons ($i = A, B, C$) and $\hbar\omega_P(\vec{k}_\parallel)$ is the energy of the cavity photons as a function of in-plane wavevector \vec{k}_\parallel . b_i is the excitonic annihilation operator, a_P is the cavity photon annihilation operator, and g_i is the coupling constant between the i -th exciton and the photon mode. Notably, to reproduce the energy dispersion of the polariton branches observed experimentally, at least three distinct excitonic states are required. The Supplementary Material contains the numerical details of the Hamiltonian employed [29].

The energy of the microcavity optical mode was designed such that the lower polariton branch has a good energetic overlap with the maximum emission of $(\text{PEA})_2\text{PbI}_4$ at small in-plane wavevectors. This design should facilitate the population of the lower polariton $\vec{k}_\parallel = \vec{0}$ state via radiative pumping [14, 15] and the observation of polariton-polariton correlations. The theoretical Q -factor of the microcavity is $Q \approx 66$, according to a transfer matrix simulation included in the Supplementary Material [29]. This corresponds to an optical mode lifetime $\tau_{\text{Opt.}} = Q/\omega_{\text{Opt.}}(\vec{k}_\parallel = \vec{0}) \approx 114$ fs. Since the lifetime of exciton-polaritons is predominantly limited by that of the microcavity optical mode, the polariton lifetime in this system should be at the shortest equal to $\tau_{\text{Opt.}}$.

B. Modified exciton reservoir dynamics due to strong light-matter coupling

Under a non-resonant excitation (2.638 eV, 200 fs), we observe that the PL arises predominantly from the lowest energy states ($|k_\parallel| < 10 \mu\text{m}^{-1}$) of the lower polariton branch, as targeted by our microcavity design, see Fig. 3(a-c). When the excitation fluence increases, the PL grows more prominently at in-plane wavevectors $|k_\parallel| < 5 \mu\text{m}^{-1}$. This is particularly clear when we plot the maximum photoluminescence intensity ($I_{\text{PL,max.}}$) as a function of excitation fluence at different \vec{k}_\parallel (Fig. 3(d)). Notice that $I_{\text{PL,max.}}$ grows the most at $\vec{k}_\parallel = \vec{0}$ (pink diamonds in Fig. 3(d)) and that it follows a sublinear trend at large in-plane wavevectors (black squares in Fig. 3(d)). The redistribution of the photoluminescence energy dispersion indicates an accumulation of the polariton population at states with small in-plane wavevectors. Nevertheless, exciton-polariton condensation is not attained in the system. It is important to highlight that the photoluminescence of $(\text{PEA})_2\text{PbI}_4$ shows a secondary feature at 2.31 eV that grows with increasing fluence (Fig. S3 [29]). This emission

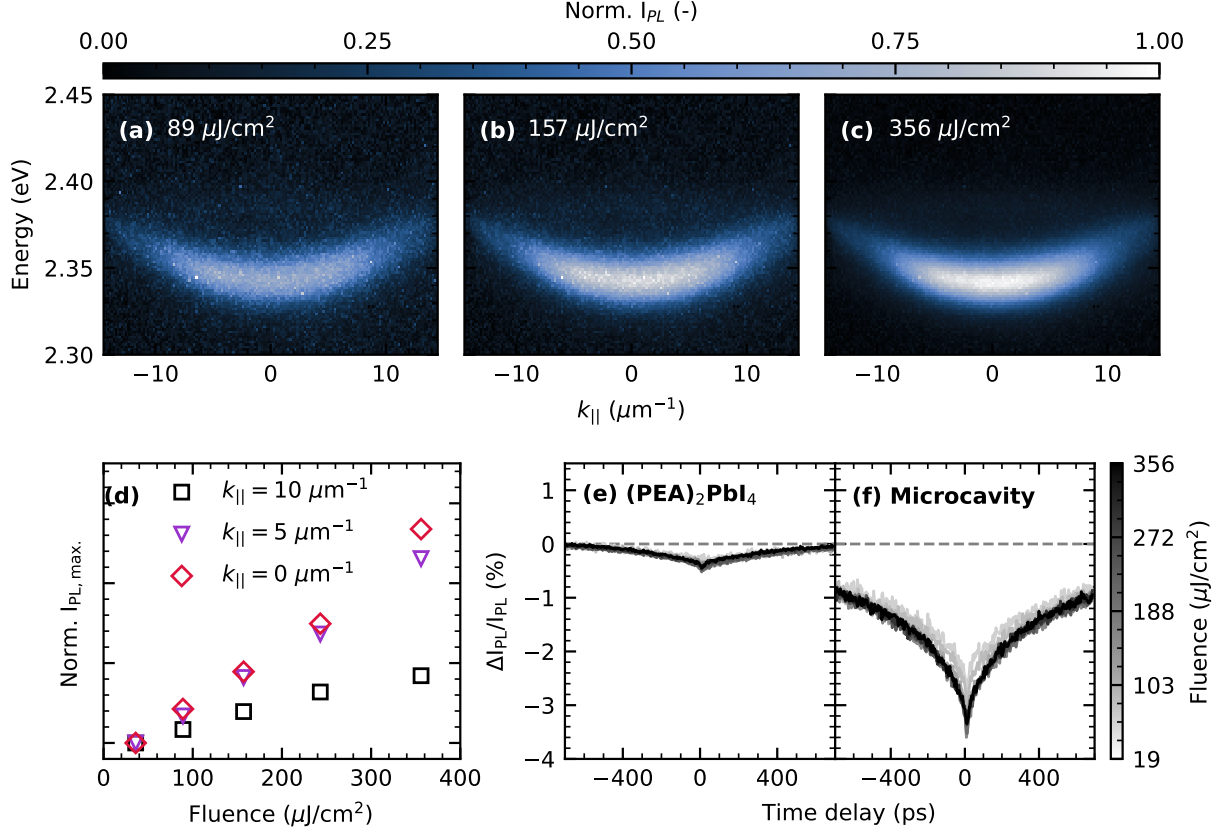


FIG. 3. Nonlinearities in the photoluminescence (PL) of the $(\text{PEA})_2\text{PbI}_4$ microcavity at 5 K under non-resonant excitation (2.638 eV, 220 ps). (a-c) Normalized photoluminescence energy dispersion at incident fluences of 89, 157, and 356 $\mu\text{J}/\text{cm}^2$. (d) The PL accumulates at small in-plane wavevectors with increasing excitation fluence. The maximum PL intensity ($I_{\text{PL,max}}$) grows at small in-plane wavevectors ($k_{||} = 0 \mu\text{m}^{-1}$ and $5 \mu\text{m}^{-1}$), and it follows a sublinear trend at $k_{||} = 10 \mu\text{m}^{-1}$. (e-f) Fraction of nonlinear PL ($\Delta I_{\text{PL}}/I_{\text{PL}}$), measured via excitation correlation photoluminescence spectroscopy (ECPL), in a bare $(\text{PEA})_2\text{PbI}_4$ film and the microcavity. The ECPL and the PL energy dispersion experiments share the same excitation and collection conditions, however, the nonlinear dynamics obtained via ECPL are not resolved along the energy or in-plane wavevector axes since we measure with a photoreceiver.

contributes to the radiative pumping of exciton-polaritons and the observed accumulation of polariton population. This secondary emission has been assigned to a dark exciton, a biexciton state, and the overlap between both [5, 15, 30]. Addressing the nature of the secondary emission feature is out of the scope of this work. However, we highlight that the

only report of polariton condensation in two-dimensional metal halide semiconductors was attained via radiative pumping of polariton states through this secondary emission [5].

We identify the incoherent nonlinear dynamics of the exciton reservoir, inherited by exciton-polaritons, through excitation correlation photoluminescence (ECPL) spectroscopy [31–33]. Using this technique, we isolate the fraction of nonlinear photoluminescence $\Delta I_{\text{PL}}/I_{\text{PL}}$, where $\Delta I_{\text{PL}} = I_{\text{PL}}(2I_{\text{pump}}) - 2I_{\text{PL}}(I_{\text{pump}})$, of the lower polariton within the timescale of the excitons’ lifetime (picoseconds) and compare it with that of excitons in a bare $(\text{PEA})_2\text{PbI}_4$ film for reference. In the $(\text{PEA})_2\text{PbI}_4$ film, we observe a small negative nonlinearity for all population times and exciton fluences, $|\Delta I_{\text{PL}}/I_{\text{PL}}| < 0.5\%$ in Fig. 3(e). Contrary, in the microcavity, we observe a negative nonlinearity one order of magnitude greater than that measured in the film, $|\Delta I_{\text{PL}}/I_{\text{PL}}| < 4\%$ in Fig. 3(f). The magnitude of the negative nonlinear PL signal is indicative of the extent of exciton-exciton annihilation in each system (see the kinetic model in the Supporting Material [29]). The more negative nonlinearity observed in the microcavity is attributed to increased exciton-exciton annihilation, evidencing the modification of the exciton reservoir dynamics in strongly coupled two-dimensional metal halides.

We rationalize the exciton-exciton annihilation increase in the microcavity as a consequence of the spatial delocalization of the exciton reservoir via population exchange with exciton-polaritons. This hypothesis goes in line with recent work in organic semiconductor microcavities reporting a rapid exchange between polaritons and the reservoir that drives exciton-polariton transport at timescales beyond the polariton lifetime [19, 34, 35]. In the context of strongly coupled two-dimensional metal halides, excitations propagating beyond the exciton-polaritons lifetime, faster and for longer distances than excitons in the semiconductor has also been reported [35, 36]. This suggests an efficient exchange between the exciton reservoir and polariton states, manifesting in our results as an increased exciton-exciton annihilation in the reservoir due to its larger propagation extent.

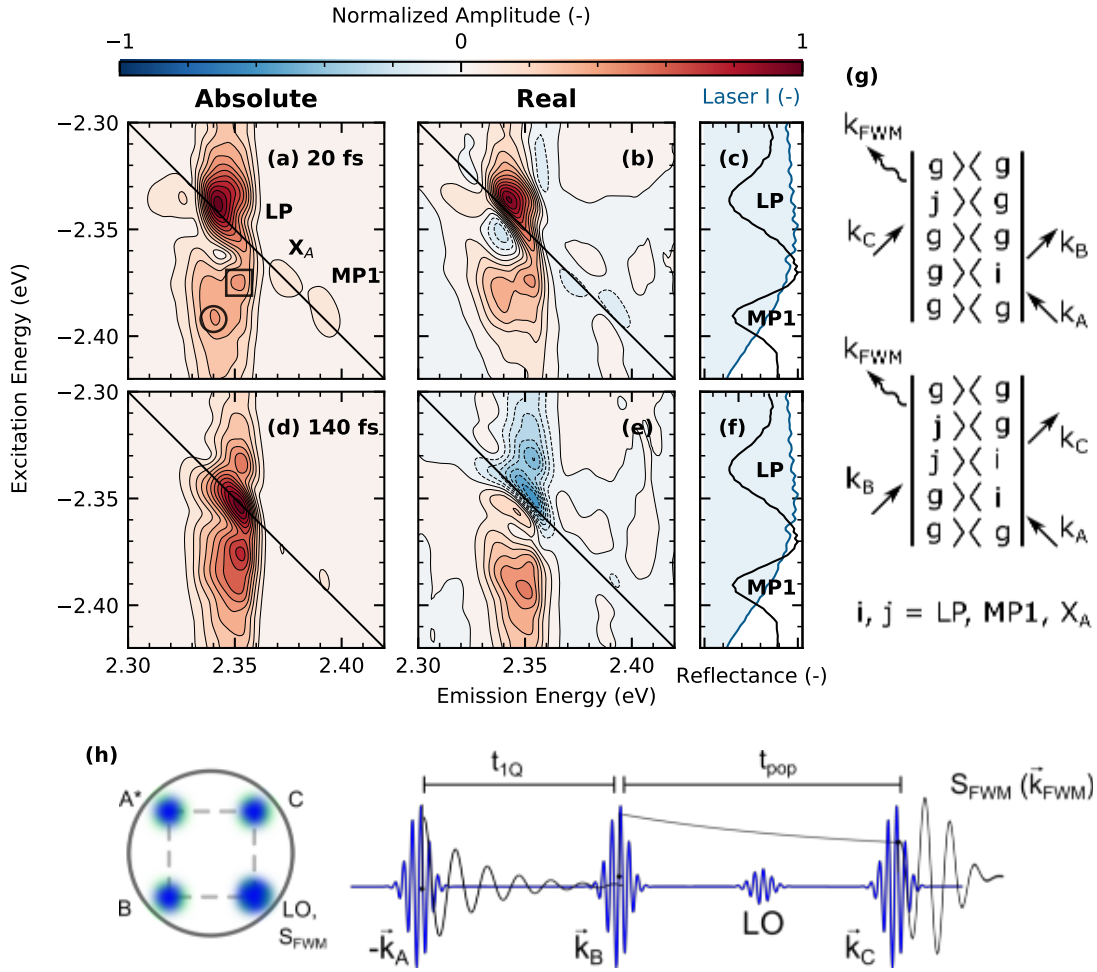


FIG. 4. Two-dimensional 1Q rephasing spectra of the $(\text{PEA})_2\text{PbI}_4$ microcavity measured at 10 K. The subfigures (a-b) correspond to the absolute and real components, respectively, at population times (t_{pop}) of 20 fs and (d-e) 140 fs. All the spectra were collected by pumping with the same laser spectrum and an incident fluence of $0.7 \mu\text{Jcm}^{-2}$ per pulse. Panels (c) and (f) show the laser spectrum used and the reflectance of the microcavity at $\vec{k} = 0$. (g) Double-sided Feynman diagrams exemplifying excitation pathways leading to the 1Q rephasing spectra. (h) In the experimental setup, the pulses are arranged in a *BoxCAR* geometry (left) and time ordered to measure the 1Q rephasing spectra (right). The pulses excite the sample at an angle of 2.3° , which corresponds to $|\vec{k}_{\parallel}| = 0.92 \mu\text{m}^{-1}$. The sequence of three \vec{k}_{\parallel} pulses generates a third-order polarization and the emission from the nonlinear polarization, at a defined wavevector \vec{k}_{FWM} , is then interfered with a co-propagating attenuated fourth pulse, acting as a local oscillator (LO) that amplifies the signal.

C. Exciton and polariton ultrafast correlations

To resolve many-body processes involving polariton states, one needs a spectroscopic experiment with a pulse duration shorter than the polariton lifetime [37] (estimated to be at the shortest $\tau_{\text{Opt.}} \approx 114$ fs in the $(\text{PEA})_2\text{PbI}_4$ microcavity). For this purpose, we used multidimensional spectroscopy with ≈ 20 fs pulses (Fig. S6 [29]) resonant with the lower and first middle polariton (LP and MP1), as well as with the X_A exciton reservoir (Figs. 4(d) and (h)). Consequently, we observe the correlations between these states, but not those involving the upper polariton (UP), the other middle polaritons (MP2 and MP3), and exciton reservoirs X_B and X_C . We show, in Figs. 4 and 5, the one-quantum (1Q) rephasing response of the microcavity collected in transmission. In 1Q experiments, we scan the time evolution of coherent states with a single-step excitation ($t_{1\text{Q}}$ in Fig. 4(h)). The result is a two-dimensional map correlating the absorption and emission energies of single-excitation transitions.

In the 1Q rephasing spectrum at early population times ($t_{\text{pop}} = 20$ fs), we observe three main features along the diagonal with energies of 2.342, 2.371, and 2.390 eV (Figs. 4(a-b)). We assign these features to the lower polariton (LP), X_A exciton reservoir, and the first middle polariton (MP1), respectively, in correspondence with the reflectance of the microcavity at $\vec{k}_{\parallel} = 0$, Fig. 4(c), and the absorption of $(\text{PEA})_2\text{PbI}_4$ (top black solid line in the left panel of Fig 2(b)). Discerning such clear features corresponding to X_A states can be rationalized through exciton-polariton models that include disorder (i.e., inhomogeneous broadening) in the exciton reservoir [38, 39], and have also been seen in two-dimensional coherent spectroscopy measurements of a strongly-coupled organic microcavity [40].

The real component of the 1Q rephasing spectra uncovers the phase behavior of the LP, X_A , and MP1 signatures. At $t_{\text{pop}} = 20$ fs (Fig 4(b)), X_A and MP1 show unambiguous dispersive lineshapes, with a π -shift difference between them. On the other hand, the phase of the lower polariton looks cluttered, possibly due to overlapping transitions [25, 41]. As population time advances to 140 fs, Fig. 4(f), the phase of the LP signature declutters, and we observe a clear dispersive lineshape with the same phase as that of MP1. Based on the literature, we interpret the dispersive lineshapes in the real part of the rephasing as excitation-induced shifts in which high densities of polaritons and excitons renormalize the energies of the system [42, 43]. Accordingly, the π -shift difference between the po-

lariton and X_A lineshapes indicates that LP and MP1 are experiencing excitation-induced blueshifts, while X_A undergoes a redshift. Blueshifts of polariton states can arise due to Rabi contraction or polariton-polariton interactions. Rabi contraction refers to the blueshift of the LP and redshift of the UP due to ground state bleaching of the exciton reservoir induced by the excitation [44]. For systems with middle polaritons, like the one described here, Rabi contraction should also lead to a blueshift of MP branches. Additionally, Fieramosca et al. [2] reported that polariton-polariton interactions in $(\text{PEA})_2\text{PbI}_4$, stemming from Coulombic effects of polariton excitonic constituents, induce blueshifts in the LP and MPs. The redshift of X_A can be related to exciton-exciton interactions or Coulomb mutual screening [24, 25, 45]. Identifying the exact mechanisms leading to these lineshapes is not straightforward. It requires modeling the 1Q rephasing spectra including polariton and exciton densities, as well as light-matter coupling and exciton-exciton interaction parameters, and it is left for future work [46].

The absolute 1Q rephasing response of the microcavity at various population times (Figs. 5 and S7 [29]) informs about the excited state population dynamics, particularly population transfer and periodic energy exchange (i.e., Rabi oscillations) amongst polariton states. We evidence that ultrafast incoherent population transfer from X_A and MP1 to the LP dominates the 1Q dynamics of the $(\text{PEA})_2\text{PbI}_4$ microcavity. Population transfer results in asymmetrical off-diagonal features like the ones marked with a square and a circle in Fig. 4(a), which indicate transfer pathways $X_A \rightarrow \text{LP}$ and $\text{MP1} \rightarrow \text{LP}$, respectively [47]. As population time progresses, the amplitudes of the asymmetrical off-diagonal peaks increase relative to the other features in the two-dimensional map (Figs. 4(e-g) and 5(b)) supporting a downhill transfer from X_A and MP1 to the LP occurring within a ≈ 100 fs timescale. Similar scenarios have been observed in organic semiconductor microcavities [40, 41]. Contrary, Rabi oscillations between the lower and upper polariton govern the 1Q response of GaAs quantum well microcavities [48].

The apparent blueshift of the on-diagonal LP feature with increasing t_{pop} (Fig. 4), emphasized by tracking the LP feature's contour (Fig 5(d)), is an indication of the LP population getting redistributed towards states with higher energy and larger \vec{k}_{\parallel} . By comparing diagonal cuts of the lower polariton at different population times (Fig 5(c)), normalized at 2.340 eV (the lower polariton energy at $\vec{k}_{\parallel} = 0$), we show that the population of higher-energy larger- \vec{k}_{\parallel} LP states grows in proportion to that of $\vec{k}_{\parallel} = 0$ as t_{pop} increases. We interpret

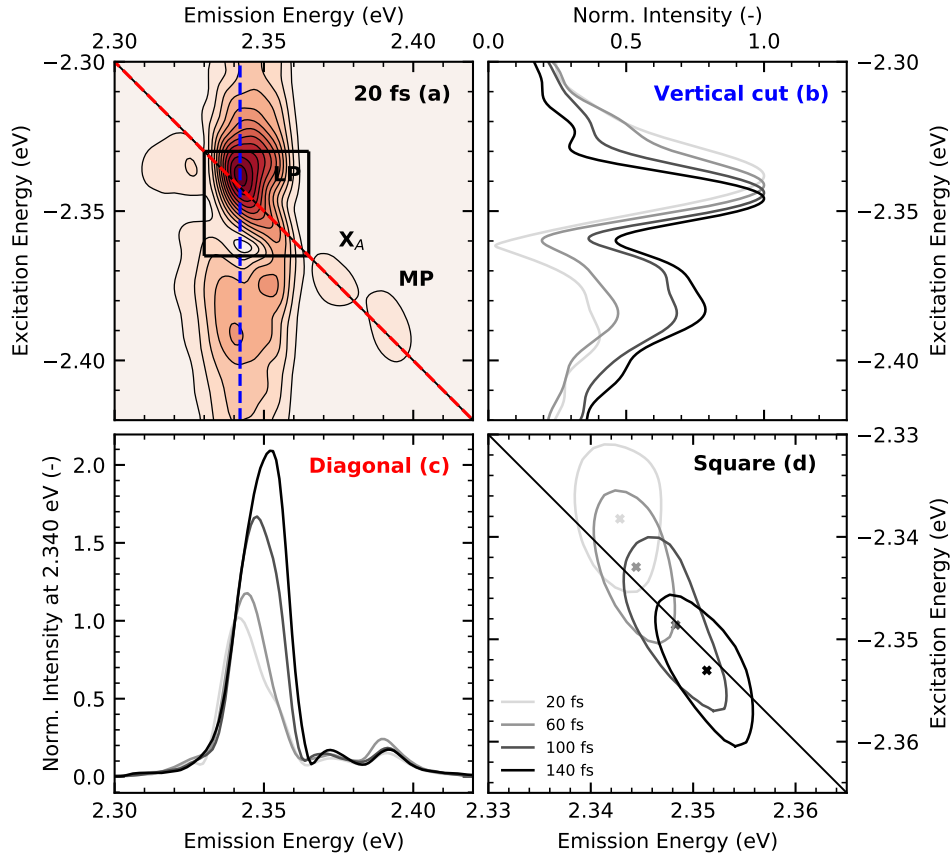


FIG. 5. Summary of the main features evolving with population time in the 1Q rephasing two-dimensional spectra. (a) The features tracked are marked in the early population time ($t_{\text{pop}} \approx 20$ fs) absolute spectrum, same as the one shown in Fig. 4(a). The blue dashed line corresponds to a cut along the emission energy axis at an energy of 2.342 eV, the red dashed line corresponds to a cut along the diagonal, and the black square corresponds to the area where the contour cuts are retrieved. Their evolution with population time is shown in (b), (c), and (d), respectively.

this population redistribution along the lower polariton branch towards states with higher energy and larger \vec{k}_{\parallel} as a depletion of the $\vec{k}_{\parallel} = 0$ LPs within a ≈ 100 fs timescale, caused by very efficient scattering. The growth of the population at higher in-plane wavevector states can have a contribution from the shorter lifetime of the LPs at $\vec{k}_{\parallel} = 0$, due to their greater photonic component (Fig. S1) [34]. Nevertheless, we don't expect this contribution to cause the depletion as the photonic component of the lower polariton at $\vec{k}_{\parallel} = 0$ and slightly larger \vec{k}_{\parallel} are very similar.

D. Scattering between polaritons and the exciton reservoir

Using two-quantum (2Q) two-dimensional spectroscopy [49, 50], we elucidate two-particle correlations between excitons and polaritons in the $(\text{PEA})_2\text{PbI}_4$ microcavity. These correlations include both bound (e.g., biexcitons and bipolaritons) and unbound two-particle states interacting via a Coulombic potential (i.e., at the mean-field level) [51, 52]. In the 2Q experiment, we utilize the pulse sequence shown in Fig. 6(f), and we scan the time evolution of coherent states $t_{2\text{Q}}$ accessed via a two-step excitation. Multi-particle correlations have been extensively studied for excitons and polaritons in GaAs quantum wells through this method [50, 52]. Takemura *et al.* [53] showed that exciton-exciton interactions lead to both self- (LP-LP, UP-UP) and cross-correlations (LP-UP, UP-LP) of the polariton branches. The self- and cross-correlations manifest in the 2Q two-dimensional map as diagonal ($E_{\text{Em.}} = 2E_{\text{Exc.}}$) and off-diagonal features respectively. As discussed before, in our experiment, we probe only the LP, X_A , and MP1 states. Since LP and MP1 polaritons have important contributions from X_A (Fig. S1), we expect two-particle states between LP, X_A , and MP1 to be mediated by X_A - X_A interactions.

In the absolute two-quantum spectra (Fig. 6(a)), we observe a feature in the diagonal ($E_{\text{Em.}} = 2E_{\text{Exc.}}$) corresponding to LP-LP self-correlations. We include the real and imaginary components of the two-quantum map in Figs. 6(b) and (c), correspondingly. The dispersive-like lineshape of the LP-LP feature in the real component of the spectrum indicates that exciton interactions at the mean-field level are the principal contributors to the nonlinear signal measured, consistent with the prediction by Karaiskaj *et al* [51]. We see an asymmetry stretching above the diagonal ($E_{\text{Em.}} = 2E_{\text{Exc.}}$) in the absolute (Fig 6(a)) and the real component of the spectra (Fig. 6(b)). We interpret this asymmetry as two closely spaced off-diagonal peaks, clearly resolved in a vertical cut at the emission energy of 2.335 eV (dashed line in Fig. 6(a) and spectrum in Fig. 6(d)). The difference between the energies of the off-diagonal and diagonal features ($E_{2\text{Q}} - E_{\text{diag}}$) are 32 and 65 meV, which correspond to the energy differences $E_{X_A} - E_{\text{LP}}$ and $E_{\text{MP1}} - E_{\text{LP}}$, respectively. This suggests that the off-diagonal features correspond to LP- X_A and LP-MP1 two-particle states, as indicated with green and purple diamonds in Figs. 6(d-e). Generally, at the emission energies E_{X_A} and E_{LP} , one expects self-interactions from X_A and MP1 in the diagonal and asymmetries below the diagonal, also corresponding to LP- X_A and LP-MP1 cross-correlations. However, the

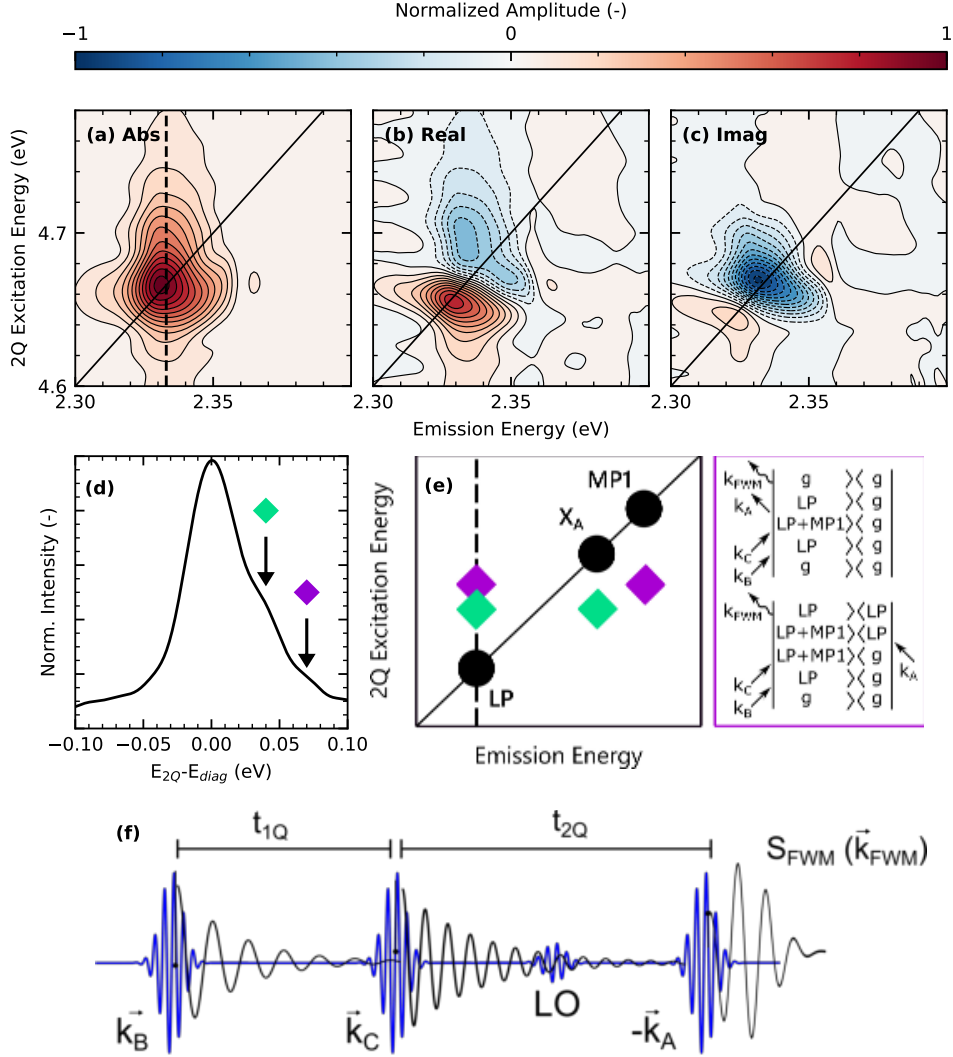


FIG. 6. Double-quantum non-rephasing 2D coherent spectra at a population time of 20 fs. The subfigures correspond to the (a) absolute, (b) real, and (c) imaginary components. The main feature observed along the $2E_{Exc.} = E_{Em.}$ diagonal indicates LP-LP interactions. (d) A cut along the emission energy axis reveals two cross-peaks with energies 40 meV (green diamond) and 70 meV (purple diamond) greater than that of LP-LP interactions. (e) Illustration of a 2Q non-rephasing spectra of a system with LP- X_A and LP-MP interactions, which manifest in cross-peaks at the energies $E_{LP} + E_{X_A}$ and $E_{LP} + E_{MP}$, as indicated with green and purple diamonds respectively. Two examples of pathways that involve LP-MP interactions and manifest as cross-peaks are included to the right. (f) Diagram showing the pulse sequence employed to measure the 2Q rephasing spectra.

nonlinear response obtained depends on the laser spectrum employed for the excitation [51], which in our case has a higher intensity at the lower polariton energy (Fig. 4(c)), exciting the LP preferentially. All the expected signatures for self- and cross-interactions between LP, X_A , and MP1, as well as exemplary 2Q pathways involving LP-MP1 correlations that give rise to cross-peaks in the double-quantum non-rephasing spectra, are summarized in Fig.6(e). Concisely, we demonstrate that both excitons (X_A) and middle polaritons (MP1) act as scattering reservoirs for the lower polariton states and play an integral part in the polariton dynamics, leading to fairly complex scattering pathways in two-dimensional metal halide microcavities. This observation further supports that the exciton reservoir plays a more active role than solely being responsible for populating polariton states.

II. DISCUSSION

In this work, we show there is an interplay between the exciton reservoir and polariton state dynamics in two-dimensional metal-halide semiconductors. And, in the context of exciton-polariton condensation, we identify mechanisms limiting the formation of polariton condensates. The exciton reservoir displays an increased exciton-exciton annihilation compared to the bare semiconductor. The latter quenches the exciton reservoir available for radiative pumping and hinders the population of lower polariton states within picosecond timescales. We propose that the increased exciton-exciton annihilation in the reservoir is a result of a longer exciton interaction radius due to delocalization, induced by the ultrafast population transfer between the exciton reservoir and exciton-polariton states. This goes in line with previous work [19, 34, 35, 40] and with our observations at shorter timescales. In the femtosecond timescale, we observe ultrafast population transfer from X_A and MP1 to the lower polariton as the mechanism dominating the one-quantum dynamics of the system, and we estimate that this transfer occurs along ≈ 100 fs. Most importantly, also within a timescale of ≈ 100 fs, we resolve a depletion of the lower polariton population from the $\vec{k} = 0$ state towards LP states with larger energy and in-plane wavevector. We suggest that this population depletion is caused by very efficient scattering that promptly expulses lower polaritons from the $\vec{k}_{\parallel} = 0$ state. Last, we characterize two-particle correlations in the system and identify X_A and MP1 as Coulomb scattering baths coupled to the lower polariton at a mean-field interaction level. We also observe strong LP-LP Coulomb scattering,

inherited from the polaritons' excitonic constituents, as the most prominent feature in the 2Q experiments. This could drive the dephasing of the lower polariton towards the exciton reservoir, as proposed by Takemura *et al* in the case of GaAs microcavities [54, 55]. We believe that the strong correlations between the exciton reservoir and exciton-polaritons in strongly coupled two-dimensional metal halide semiconductors, as well as the mechanisms limiting polariton condensation identified here, can be generalized to hybrid semiconductors with ionic lattices and electron-phonon coupling.

III. METHODS

(PEA)₂PbI₄ microcavity preparation

The microcavity comprises a bottom quarter-wavelength distributed Bragg reflector (DBR) with 10.5 pairs of TiO₂/SiO₂, a 60 nm (PEA)₂PbI₄ spin-coated film, a 125 nm poly(methyl methacrylate) (PMMA) spacer, and a top 40 nm silver mirror. The DBR has a stopband centered at 520 nm and was purchased from SpectrumThinFilms. For the microcavity preparation, first, we cleaned the DBR in sequential ultrasonic baths of acetone and IPA for 15 min each. Then, we dried it with nitrogen and treated it with UV-ozone for 15 min. The perovskite precursor solutions were prepared by dissolving PbI₂ (purity > 99.99%) and phenethylammonium iodide (purity > 99.99%) in N,N-Dimethylformamide (purity > 99.98%) at a 0.13 M concentration. The perovskite films were deposited by dropping 80 μ L of precursor solution on the 2.54 cm⁻² clean DBRs before spin coating them at 6000 rpm for 30 s with an acceleration of 6000 rpm/s. Immediately after, the perovskite films were annealed for 10 min at 100 °C. The PMMA solution was prepared by dissolving 30 mg of PMMA (Mw \sim 15,000 g/mol) in 1 mL of toluene (purity > 99.98%). The PMMA solution was then deposited by spin coating. 80 μ L of the solution were dropped on the perovskite layer and spin-coated employing a 2-step process, with an initial spreading step at 100 rpm accelerated at 1000 rpm/s for 10 s, followed by a 6000 rpm step accelerated at 6000 rpm/s. The stack was heated up for 5 minutes at 60 °C to dry the PMMA film. Physical vapor deposition (PVD) was used for the top silver mirror, silver pellets (purity > 99.999%) were thermally evaporated at a rate of 0.5 Å/s to a final thickness of 42 nm.

Fourier Microscopy

We imaged the energy dispersion of the reflectance and photoluminescence using a Fourier microscope. The microscope employs a Zeiss LD EC Epiplan Neofluar 100X infinity-corrected objective ($NA = 0.75$), an Acton SpectraPro 300i spectrometer, and an Andor Newton EM camera. For reflectance and photoluminescence measurements, we use a Thorlabs SLS201L broadband light source and the output of a commercial optical parametric amplifier (ORPHEUS, Light Conversion) at 470 nm (2.64 eV), respectively.

Excitation correlation photoluminescence (ECPL)

The excitation correlation photoluminescence setup uses as a laser source a PHAROS (Model PH1-20-0200-02-10, Light Conversion) which outputs 220 fs pulses at a wavelength of 1030 nm and with a repetition rate of 100 kHz. A portion of the laser beam is sent into a commercial optical parametric amplifier (ORPHEUS, Light Conversion) which then outputs 470 nm (2.64 eV). The pulse trains are then split 50/50 by a beam splitter cube, and one of the pulse trains is directed to a motorized linear stage (LTS300, Thorlabs), to impart a time delay between the two pulses. Both pulses are amplitude-modulated with a chopper at distinct frequencies (522 and 700 Hz). The pulses are then recombined and focused onto the sample using the same setup described in the Fourier Microscopy section. A flip mirror allows us to alternate between the camera to measure the photoluminescence energy dispersion and an avalanche photodiode (APD440A, Thorlabs) for the ECPL experiment. The total integrated response is demodulated, using a lock-in amplifier (HF2LI, Zurich Instruments), at the fundamental and sum of the modulation frequencies to isolate the linear and nonlinear components of the photoluminescence. detection (ECPL).

Two dimensional coherent spectroscopy

A detailed description of the setup implemented can be found in our previous work [22, 23]. Briefly, a portion of the 1030 nm, 220 fs output of the PHAROS at a 100-kHz repetition rate is directed into a home-built third-harmonic-pumped non-collinear optical parametric amplifier. Four pulses in BoxCAR geometry are generated using a diffractive optical element. The four pulses are then sent to a home-built pulse shaper which compresses the

pulses individually using a second harmonic generation chirp scan. Additionally, the pulse shaper applies a delay between the pulses and performs the phase cycle during the measurement. The resulting pulse duration was 20 fs full-width at half-maximum, measured by second-harmonic generation cross-frequency-resolved optical gating (SHG-XFROG). All measurements were carried out in a vibration-free closed-cycle cryostat (Montana Instruments). The spot size was $95 \pm 5 \mu\text{m}$.

ACKNOWLEDGMENTS

The design and fabrication of the microcavity, the Fourier microscopy, the ECPL measurements, and the writing of the corresponding manuscript sections by VQC, ERG, MGD, CARP, JPCB, and CSA were supported by the National Science Foundation Science and Technology Center (STC) for Integration of Modern Optoelectronic Materials on Demand (IMOD) under award number DMR-2019444. The optical instrumentation for the two-dimensional coherent spectroscopy was supported by the National Science Foundation (DMR-1904293). The two-dimensional coherent spectroscopy experiments and the redaction of the corresponding manuscript sections by VQC, ERG, and CSA were supported by the National Science Foundation (DMR-2019444). VQC thanks the Georgia Tech Quantum Alliance and SPIE Optics and Photonics Education Scholarships for graduate student support. CARP acknowledges the support of the National Aeronautics and Space Administration (Award#80NSSC19M0201) The theoretical contribution by ERB was funded by the National Science Foundation (CHE-2102506) and the Robert A. Welch Foundation (E-1337). ARSK acknowledges start-up funds from Wake Forest University, funding from the Center for Functional Materials, and funding from the Office of Research and Sponsored Programs at Wake Forest University. HL and CSA acknowledge funding from the Government of Canada (Canada Excellence Research Chair CERC-2022-00055) and the Courtois Institute, Faculté des arts et des sciences, Université de Montréal (Chaire de Recherche de l'Institut Courtois).

AUTHOR CONTRIBUTIONS

VQC and ERG contributed equally to this work and should be considered first co-authors. The microcavities were designed and prepared by MGD and VQC under the supervision of CARP, NS, and JPCB. VQC and ERG performed the nonlinear spectroscopy measurements and analysis under the supervision of ARSK and CSA. HL and ERB developed the theoretical analysis. VQC and ERG wrote the original draft, supervised by ARSK and CSA, and all co-authors contributed to the final draft of the manuscript. ARSK and CSA are corresponding co-authors; CSA is the submitting author.

-
- [1] E. Togan, H.-T. Lim, S. Faelt, W. Wegscheider, and A. Imamoglu, *Phys. Rev. Lett.* **121**, 227402 (2018).
 - [2] A. Fieramosca, L. Polimeno, V. Ardizzone, L. D. Marco, M. Pugliese, V. Maiorano, M. D. Giorgi, L. Dominici, G. Gigli, D. Gerace, D. Ballarini, and D. Sanvitto, *Science Advances* **5**, eaav9967 (2019).
 - [3] J. Kasprzak, M. Richard, S. Kundermann, A. Baas, P. Jeambrun, J. M. J. Keeling, F. M. Marchetti, M. H. Szymańska, R. André, J. L. Staehli, V. Savona, P. B. Littlewood, B. Deveaud, and L. S. Dang, *Nature* **443**, 409 (2006).
 - [4] R. Balili, V. Hartwell, D. Snoke, L. Pfeiffer, and K. West, *Science* **316**, 1007 (2007).
 - [5] L. Polimeno, A. Fieramosca, G. Lerario, M. Cinquino, M. De Giorgi, D. Ballarini, F. Todisco, L. Dominici, V. Ardizzone, M. Pugliese, C. T. Prontera, V. Maiorano, G. Gigli, L. De Marco, and D. Sanvitto, *Advanced Optical Materials* **8**, 2000176 (2020).
 - [6] H. Deng, G. Weihs, D. Snoke, J. Bloch, and Y. Yamamoto, *PNAS* **100**, 15318 (2003).
 - [7] C. P. Dietrich, A. Steude, L. Tropic, M. Schubert, N. M. Kronenberg, K. Ostermann, S. Höfling, and M. C. Gather, *Sci. Adv.* **2**, e1600666 (2016).
 - [8] J. Gu, B. Chakraborty, M. Khatoniari, and V. M. Menon, *Nat. Nanotechnol.* **14**, 1024 (2019).
 - [9] A. Mischok, S. Hillebrandt, S. Kwon, and M. C. Gather, *Nat. Photonics* **17**, 393 (2023).
 - [10] D. Ballarini, M. De Giorgi, E. Cancellieri, R. Houdré, E. Giacobino, R. Cingolani, A. Bramati, G. Gigli, and D. Sanvitto, *Nat. Commun.* **4**, 1778 (2013).

- [11] A. V. Zasedatelev, A. V. Baranikov, D. Urbonas, F. Scafrimuto, U. Scherf, T. Stöferle, R. F. Mahrt, and P. G. Lagoudakis, *Nature Photonics* **13**, 378 (2019).
- [12] T. Boulier, M. J. Jacquet, A. Maître, G. Lerario, F. Claude, S. Pigeon, Q. Glorieux, A. Amo, J. Bloch, A. Bramati, and E. Giacobino, *Adv. Quantum Technol.* **3**, 2000052 (2020).
- [13] R. T. Grant, P. Michetti, A. J. Musser, P. Gregoire, T. Virgili, E. Vella, M. Cavazzini, K. Georgiou, F. Galeotti, C. Clark, J. Clark, C. Silva, and D. G. Lidzey, *Advanced Optical Materials* **4**, 1615 (2016).
- [14] P. Deshmukh, L. Zhao, S. Satapathy, M. Khatoniar, B. Datta, B. P. Rand, and V. Menon, *Opt. Mater. Express* **13**, 1655 (2023).
- [15] M. Laitz, A. E. K. Kaplan, J. Deschamps, U. Barotov, A. H. Proppe, I. García-Benito, A. Osherov, G. Grancini, D. W. deQuilettes, K. A. Nelson, M. G. Bawendi, and V. Bulović, *Nature Communications* **14**, 2426 (2023).
- [16] M. Maragkou, A. J. D. Grundy, T. Ostatnický, and P. G. Lagoudakis, *Applied Physics Letters* **97**, 111110 (2010).
- [17] N. Somaschi, L. Mouchliadis, D. Coles, I. E. Perakis, D. G. Lidzey, P. G. Lagoudakis, and P. G. Savvidis, *Applied Physics Letters* **99**, 143303 (2011).
- [18] D. M. Coles, P. Michetti, C. Clark, W. C. Tsoi, A. M. Adawi, J.-S. Kim, and D. G. Lidzey, *Advanced Functional Materials* **21**, 3690 (2011).
- [19] R. Pandya, A. Ashoka, K. Georgiou, J. Sung, R. Jayaprakash, S. Renken, L. Gai, Z. Shen, A. Rao, and A. J. Musser, *Advanced Science* **9**, 2105569 (2022).
- [20] P. Schwendimann and A. Quattropani, *Phys. Rev. B* **77**, 085317 (2008).
- [21] M. Pieczarka, E. Estrecho, M. Boozarjmehr, O. Bleu, M. Steger, K. West, L. N. Pfeiffer, D. W. Snoke, J. Levinsen, M. M. Parish, A. G. Truscott, and E. A. Ostrovskaya, *Nature Communications* **11**, 429 (2020).
- [22] F. Thouin, S. Neutzner, D. Cortecchia, V. A. Dragomir, C. Soci, T. Salim, Y. M. Lam, R. Leonelli, A. Petrozza, A. R. S. Kandada, and C. Silva, *Phys. Rev. Materials* **2**, 034001 (2018).
- [23] F. Thouin, D. Cortecchia, A. Petrozza, A. R. Srimath Kandada, and C. Silva, *Phys. Rev. Res.* **1**, 032032 (2019).
- [24] A. R. Srimath Kandada, H. Li, F. Thouin, E. R. Bittner, and C. Silva, *The Journal of Chemical Physics* **153**, 164706 (2020).

- [25] E. Rojas-Gatjens, H. Li, A. Vega-Flick, D. Cortecchia, A. Petrozza, E. R. Bittner, A. R. Srimath Kandada, and C. Silva-Acuña, *The Journal of Physical Chemistry C* **127**, 21194 (2023).
- [26] A. R. Srimath Kandada and C. Silva, *The Journal of Physical Chemistry Letters* **11**, 3173 (2020).
- [27] D. B. Straus and C. R. Kagan, *Annu. Rev. Phys. Chem.* **73**, 403 (2022), PMID: 35119942, <https://doi.org/10.1146/annurev-physchem-082820-015402>.
- [28] M. Dyksik, D. Beret, M. Baranowski, H. Duim, S. Moyano, K. Posmyk, A. Mlayah, S. Adjokatsé, D. K. Maude, M. A. Loi, P. Puech, and P. Plochocka, *Advanced Science* **11**, 2305182 (2024).
- [29] See Supplemental Material at [URL will be inserted by publisher].
- [30] T. Kondo, T. Azuma, T. Yuasa, and R. Ito, *Solid State Communications* **105**, 253 (1998).
- [31] M. B. Johnson, T. C. McGill, and A. T. Hunter, *Journal of Applied Physics* **63**, 2077 (1988).
- [32] A. R. Srimath Kandada, S. Neutzner, V. D’Innocenzo, F. Tassone, M. Gandini, Q. A. Akkerman, M. Prato, L. Manna, A. Petrozza, and G. Lanzani, *Journal of the American Chemical Society* **138**, 13604 (2016).
- [33] E. Rojas-Gatjens, K. M. Yallum, Y. Shi, Y. Zheng, T. Bills, C. A. R. Perini, J.-P. Correa-Baena, D. S. Ginger, N. Banerji, and C. Silva-Acuña, *J. Phys. Chem. C* **127**, 15969 (2023).
- [34] G. Groenhof, C. Climent, J. Feist, D. Morozov, and J. J. Toppari, *The Journal of Physical Chemistry Letters* **10**, 5476 (2019).
- [35] L. Jin, A. D. Sample, D. Sun, Y. Gao, S. Deng, R. Li, L. Dou, T. W. Odom, and L. Huang, *ACS Photonics* **10**, 1983 (2023).
- [36] D. Xu, A. Mandal, J. M. Baxter, S.-W. Cheng, I. Lee, H. Su, S. Liu, D. R. Reichman, and M. Delor, *Nature Communications* **14**, 3881 (2023).
- [37] T. Virgili, D. Coles, A. M. Adawi, C. Clark, P. Michetti, S. K. Rajendran, D. Brida, D. Polli, G. Cerullo, and D. G. Lidzey, *Phys. Rev. B* **83**, 245309 (2011).
- [38] R. Houdré, R. P. Stanley, and M. Ilegems, *Phys. Rev. A* **53**, 2711 (1996).
- [39] T. Khazanov, S. Gunasekaran, A. George, R. Lomlu, S. Mukherjee, and A. J. Musser, *Chemical Physics Reviews* **4**, 041305 (2023).
- [40] L. Mewes, M. Wang, R. A. Ingle, K. Börjesson, and M. Chergui, *Communications Physics* **3**, 157 (2020).

- [41] M. Son, Z. T. Armstrong, R. T. Allen, A. Dhavamani, M. S. Arnold, and M. T. Zanni, *Nature Communications* **13**, 7305 (2022).
- [42] X. Li, T. Zhang, C. N. Borca, and S. T. Cundiff, *Phys. Rev. Lett.* **96**, 057406 (2006).
- [43] T. Yagafarov, D. Sannikov, A. Zasedatelev, K. Georgiou, A. Baranikov, O. Kyriienko, I. Shelykh, L. Gai, Z. Shen, D. Lidzey, and P. Lagoudakis, *Communications Physics* **3**, 18 (2020).
- [44] C. A. DelPo, B. Kudisch, K. H. Park, S.-U.-Z. Khan, F. Fassioi, D. Fausti, B. P. Rand, and G. D. Scholes, *The Journal of Physical Chemistry Letters* **11**, 2667 (2020).
- [45] K. Xiao, T. Yan, C. Xiao, F. ren Fan, R. Duan, Z. Liu, K. Watanabe, T. Taniguchi, W. Yao, and X. Cui, “Exciton-exciton interaction in monolayer mose₂ from mutual screening of coulomb binding,” (2023), arXiv:2308.14362 [cond-mat.mtrl-sci].
- [46] S. Mukamel and D. Abramavicius, *Chemical Reviews* **104**, 2073 (2004).
- [47] K. Hao, L. Xu, P. Nagler, A. Singh, K. Tran, C. K. Dass, C. Schüller, T. Korn, X. Li, and G. Moody, *Nano Letters* **16**, 5109 (2016).
- [48] J. Paul, H. Rose, E. Swagel, T. Meier, J. K. Wahlstrand, and A. D. Bristow, *Phys. Rev. B* **105**, 115307 (2022).
- [49] L. Yang and S. Mukamel, *Phys. Rev. B* **77**, 075335 (2008).
- [50] P. Wen, G. Christmann, J. J. Baumberg, and K. A. Nelson, *New Journal of Physics* **15**, 025005 (2013).
- [51] D. Karaiskaj, A. D. Bristow, L. Yang, X. Dai, R. P. Mirin, S. Mukamel, and S. T. Cundiff, *Phys. Rev. Lett.* **104**, 117401 (2010).
- [52] K. W. Stone, D. B. Turner, K. Gundogdu, S. T. Cundiff, and K. A. Nelson, *Accounts of Chemical Research* **42**, 1452 (2009).
- [53] N. Takemura, S. Trebaol, M. D. Anderson, V. Kohnle, Y. Léger, D. Y. Oberli, M. T. Portella-Oberli, and B. Deveaud, *Phys. Rev. B* **92**, 125415 (2015).
- [54] N. Takemura, M. D. Anderson, S. Biswas, M. Navadeh-Toupchi, D. Y. Oberli, M. T. Portella-Oberli, and B. Deveaud, *Phys. Rev. B* **94**, 195301 (2016).
- [55] N. Takemura, M. D. Anderson, S. Trebaol, S. Biswas, D. Y. Oberli, M. T. Portella-Oberli, and B. Deveaud, *Phys. Rev. B* **92**, 235305 (2015).

**Supplemental Material: Strong exciton-polariton correlations
shape the many-body polariton dynamics in two-dimensional
metal halide semiconductor microcavities: Competitive pathways
for polariton condensation**

Victoria Quirós-Cordero, Esteban Rojas-Gatjens, Martín Gómez-Dominguez, Hao Li,
Carlo A.R. Perini, Natalie Stingelin, Eric R. Bittner, Juan-Pablo Correa-Baena,
Ajay Ram Srimath Kandada, Carlos Silva-Acuña

S1. SIMULATIONS

a. Multiple exciton Hamiltonian

The multiple exciton Hamiltonian that describes the polariton branches observed in the microcavity energy dispersion is based on a Jaynes-Cummings model extended to three excitonic states and using the rotating wave approximation. The Hamiltonian is shown in the main text in equations (1) and (2). We diagonalized the Hamiltonian using the numerical package, Qutip [1], and leveraged the dispersion bands to estimate coupling strengths $g_{A,B,C} = 80, 80, 90$ meV. During this process, we fixed the energy of the excitonic transitions (2.370, 2.404, and 2.445 eV) and the microcavity dispersion (calculated using the transfer matrix model as described next) while changing the coupling strengths. We want to emphasize that since we have three coupling strengths as variables, various combinations of them reproduce the polariton branches observed with good accuracy, and hence these coupling strengths shouldn't be taken as definitive. However, we note that the couplings are of the order of ≈ 80 -100 meV and that at least three excitons are required to reproduce all polariton band energies. The simulated polariton eigenstates are shown in Fig. 1 as solid white lines overlaid to the experimental energy dispersion at 5 K.

Additionally in Fig. S1, we show the Hopfield coefficients for the polariton states that diagonalize the Hamiltonian. These coefficients provide information on the photonic and excitonic components making up each state.

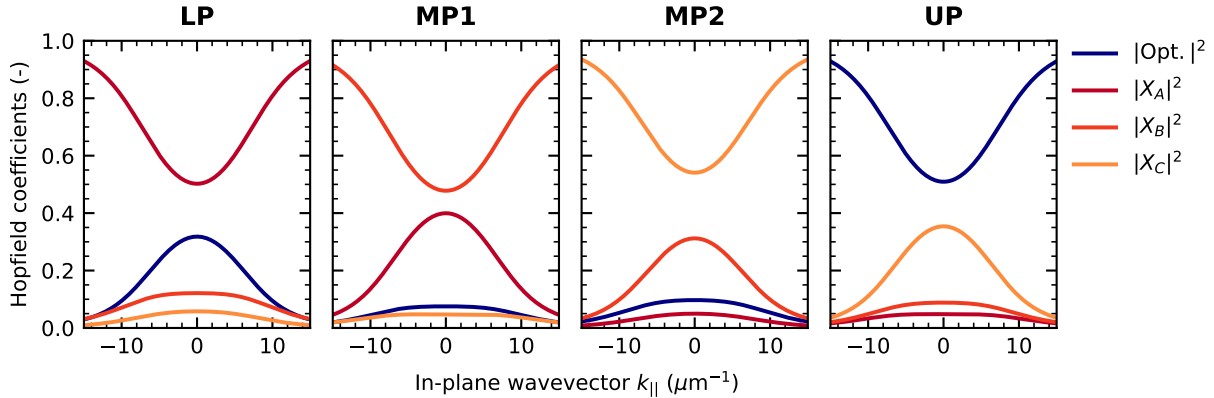


FIG. S1. Hopfield coefficients of the polariton eigenstates.

b. Transfer matrix model of the microcavity optical mode

We simulated the energy dispersion of the microcavity optical mode using a transfer matrix model (TMM). We followed the TMM equations (4)-(9) described below and used the experimentally determined thicknesses and complex energy-dependent refractive indices of every layer in the microcavity stack, except for the $(\text{PEA})_2\text{PbI}_4$. To simulate the dispersion of the optical mode, instead of that of the polariton branches via TMM, we must consider the refractive index of $(\text{PEA})_2\text{PbI}_4$ to be static, real, and equal 2.61, which is the real refractive index of the material at the target optical mode energy of 2.436 eV. The simulated dispersion of the optical mode is shown in Fig. S2. We obtained equation (3) describing the dispersion as a function of in-plane wavevector by fitting a polynomial to the reflectance minimum (red dashed line in Fig. S2)

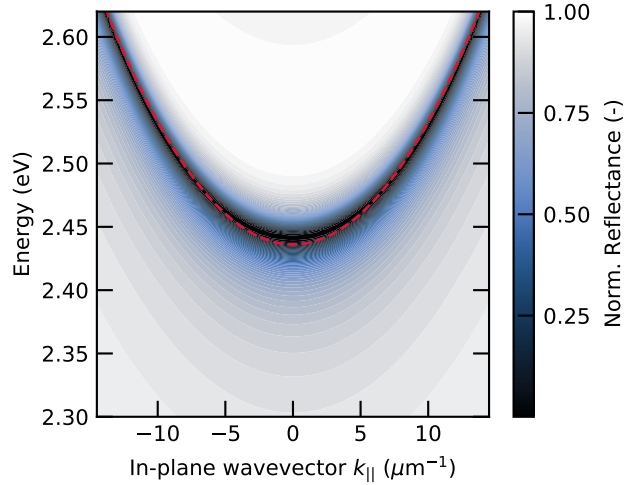


FIG. S2. Transfer matrix model of the microcavity optical mode and quadratic polynomial (red dashed line) describing the simulated dispersion.

$$E_{\text{Opt.}}(\vec{k}_{\parallel}) = \hbar\omega_P(\vec{k}_{\parallel}) = 2.436 + 9.679 \times 10^{-4} \vec{k}_{\parallel}^2 \text{ eV} \quad (3)$$

Next, we summarize the main equations of the transfer matrix model. More details can be found in Ref. [2]. The optical response of a thin film can be fully described by a transfer matrix that summarizes the continuity conditions of the electric and magnetic field components that are tangential to the film's interfaces. The angle-dependent transfer matrix of a single film is given by:

$$T_{\text{film}, s\text{-pol}} = \begin{pmatrix} \cos(\delta_{\text{film}}) & i \sin(\delta_{\text{film}})/[n_{\text{film}} \cos(\theta_{\text{film}})] \\ in_{\text{film}} \sin(\delta_{\text{film}}) \cos(\theta_{\text{film}}) & \cos(\delta_{\text{film}}) \end{pmatrix} \quad (4)$$

$$T_{\text{film}, p\text{-pol}} = \begin{pmatrix} \cos(\delta_{\text{film}}) & i \sin(\delta_{\text{film}}) \cos(\theta_{\text{film}})/n_{\text{film}} \\ in_{\text{film}} \sin(\delta_{\text{film}})/\cos(\theta_{\text{film}}) & \cos(\delta_{\text{film}}) \end{pmatrix} \quad (5)$$

$$\delta_{\text{film}} = \frac{2\pi n_{\text{film}} d_{\text{film}}}{\lambda} \cos(\theta_{\text{film}}) \quad (6)$$

Where n_{film} corresponds to the complex energy-dependent refractive index, θ_{film} is the angle of propagation of light as given by Snell's law, and d_{film} the film thickness. This result can be extended to an assembly of q thin films, where the total transfer matrix is the product of the individual matrices. The left-most matrix corresponds to the first film light traverses.

$$T_{\text{assembly}} = \prod_{\text{film}}^q T_{\text{film}} \quad (7)$$

The reflectance (R) of a thin-film assembly can then be obtained from its transfer matrix as follows:

$$\begin{pmatrix} E_{\text{in}}/E_{\text{out}} \\ H_{\text{in}}/H_{\text{out}} \end{pmatrix} = \begin{pmatrix} B \\ C \end{pmatrix} = T_{\text{assembly}} \begin{pmatrix} 1 \\ n_s \end{pmatrix} \quad (8)$$

$$R = \left(\frac{n_0 B - C}{n_0 B + C} \right) \left(\frac{n_0 B - C}{n_0 B + C} \right)^* \quad (9)$$

Where n_0 and n_s correspond to the refractive indices of the incident and output media (typically air and the substrate, correspondingly).

S2. PHOTOLUMINESCENCE

a. Linear measurements

We show the fluence-dependent photoluminescence (PL) spectra of the bare (PEA)₂PbI₄ film as a function of fluence (Fig S3). Additionally, we include the PL energy dispersion of

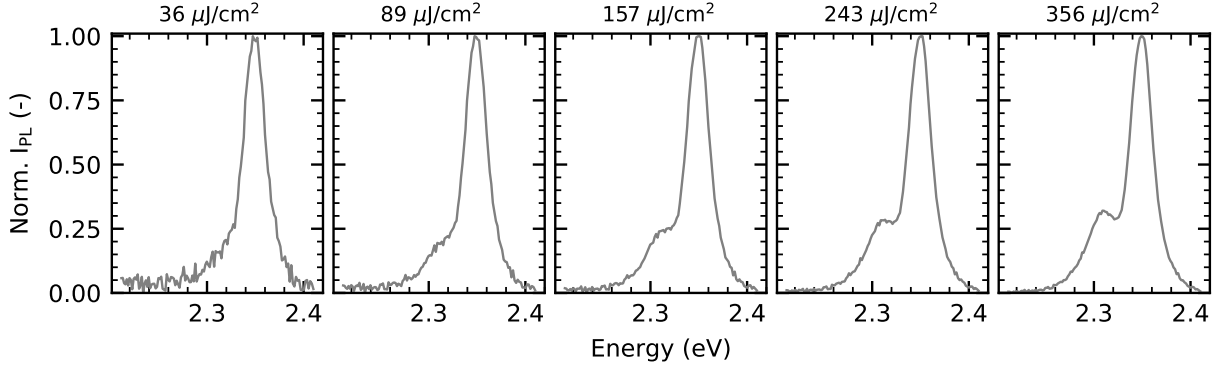


FIG. S3. Photoluminescence spectra as a function of fluence of a 60 nm $(\text{PEA})_2\text{PbI}_4$ film measured under non-resonant excitation (470 nm, 220 fs).

the lower polariton and a spectral cut at $\vec{k}_{\parallel} = 0$ (Fig. S4, top panel) as a function of fluence. These measurements were taken under non-resonant pumping (470 nm, 220 fs), using the same laser pulse employed in the ECPL experiments, and detecting with an Andor Newton EM camera. We also display the linewidth and the maximum peak energy of the lower polariton emission as a function of fluence, extracted from Lorentzian fits to the spectra (Fig. S4, bottom panel).

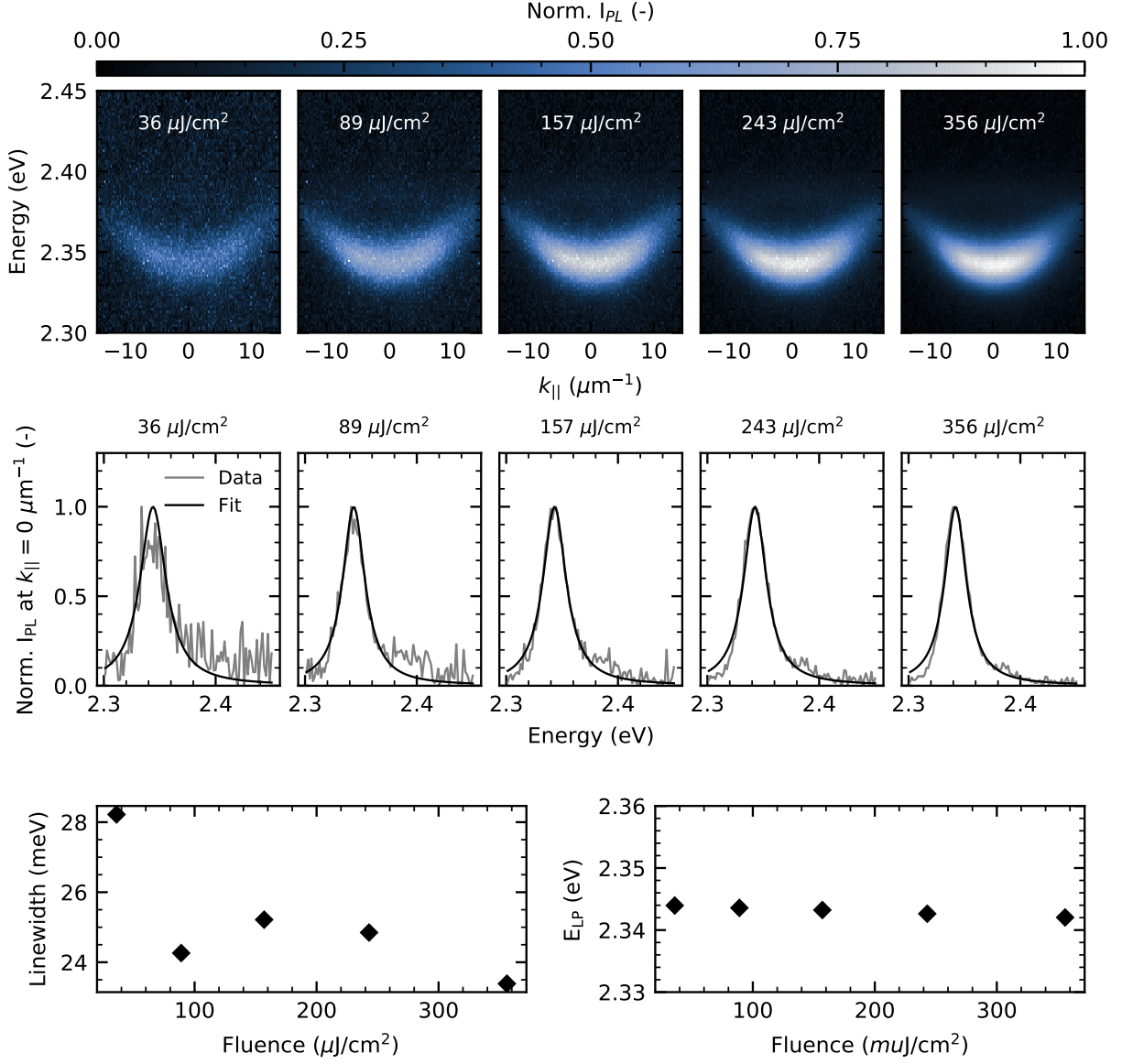


FIG. S4. Photoluminescence (PL) energy dispersion of the lower polariton, PL spectra at $\vec{k}_{\parallel} = 0$, linewidth, and energy as a function of fluence measured under non-resonant excitation (470 nm, 220 fs).

b. Nonlinear measurements: Excitation correlation photoluminescence (ECPL) spectroscopy

Briefly, ECPL is a technique that excites the sample with two pulses, one of which is temporally delayed from the other. The pulses are amplitude-modulated at two distinct frequencies (Ω_1 and Ω_2). Then, we detect the time-integrated photoluminescence and iso-

late its nonlinear component by demodulating at the sum frequency ($\Omega_1 + \Omega_2$) via lock-in detection. The time resolution arises from the delay between the two pulses.

1. Exciton-exciton annihilation model

Here, we show a simple kinetic model for exciton dynamics which includes a monomolecular recombination term with a γ rate and an exciton-exciton annihilation term with a parameter β . The differential equation and its corresponding solution are:

$$\frac{dn}{dt} = -\gamma n - \beta n^2, \quad n(t) = \frac{n_0 \gamma / \beta}{(n_0 + \gamma / \beta) \exp(\gamma t) - n_0}. \quad (10)$$

From the solution for the exciton dynamics, we can obtain the total photoluminescence after the interaction with two laser pulses, assumed to be delta functions and therefore considered as initial conditions. The total photoluminescence detected is:

$$I_{Total\ PL} \propto \int_0^\tau n_1(t) dt + \int_\tau^\infty n_2(t - \tau) dt. \quad (11)$$

The first integral considers the time when only one pulse had arrived at the sample and the second integral considers the time after the two pulses had arrived. The initial conditions correspond to $n_1(0) = n_0$ and for $n_2(0) = n_1(\tau) + n_0$. $n_1(\tau)$ is the residual population due to the sample's interaction with the first pulse. Then we subtract the single pulse contributions, $I = 2 \int_0^\infty n(t) dt = 2n_0$, to obtain the nonlinear contribution to the photoluminescence:

$$\Delta I_{PL}(\tau) \propto \ln \left(1 - \frac{\alpha^2 \exp(-\gamma\tau)}{(1 + \alpha)^2} \right); \quad \alpha = \frac{n_0 \beta}{\gamma}. \quad (12)$$

Note that although both time-resolved photoluminescence and ECPL follow the same population, their decay functions are different and we cannot compare their decay traces directly.

S3. TWO-DIMENSIONAL COHERENT SPECTROSCOPY

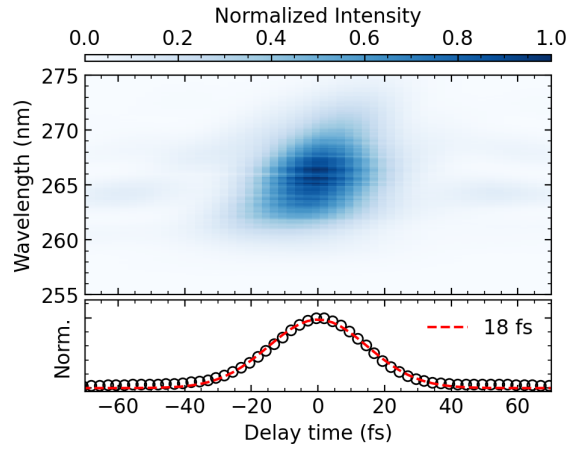


FIG. S5. X-Frog characterization of the pulse duration fitted to a Gaussian function.

-
- [1] J. Johansson, P. Nation, and F. Nori, *Computer Physics Communications* **184**, 1234 (2013).
- [2] H. A. Macleod, *Thin-Film Optical Filters (5th Ed.)* (CRC Press, 2017).